Supplementary Information

A plasmonic mesoporous gold-based SERS-microfluidic platform for the detection of infectious diseases

Mostafa Kamal Masud,[a] Daigo Natsuhara,*[b] Yuchen Dai,[a] Javeria Bashir,[a] Asep Sugih Nugraha,[a] Saad M. Alshehri,[c] Yoshio Bando,[c,d] Md Shahriar Hossain,[a,e] Yusuf Valentino Kaneti,[a] Takayuki Shibata,*[f] Yusuke Yamauchi*[a,b,g]

[a]*Australian Institute for Bioengineering and Nanotechnology (AIBN), The University of Queensland, St. Lucia, QLD 4072, Australia*

[b]*Department of Materials Process Engineering Graduate School of Engineering, Nagoya University, Nagoya, 464-8603, Japan*

[c]*Department of Chemistry, College of Science, King Saud University, Riyadh 11451, Saudi Arabia*

[d]*Australian Institute for Innovative Materials, University of Wollongong, North Wollongong, New South Wales, Australia*

[e]*School of Mechanical and Mining Engineering, Faculty of Engineering, Architecture, and Information Technology (EAIT), The University of Queensland, St Lucia, QLD, 4072, Australia*

[f]*Department of Mechanical Engineering, Toyohashi University of Technology, Aichi 441-8580, Japan.*

[g]*Department of Chemical and Biomolecular Engineering, Yonsei University, 50 Yonseiro, Seodaemun-gu, Seoul, 03722, Republic of Korea.*

Supplementary Figures

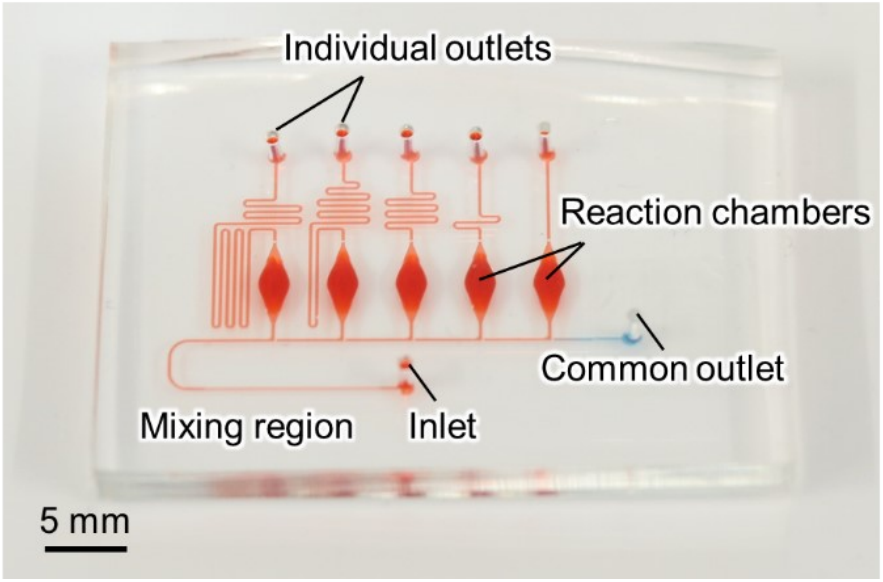

Figure S1. Schematic diagram of the microfluidic device used for the SERS detection of infectious disease. The fabricated PDMS microfluidic device consists of an array of five microchambers filled with a red-colored water.

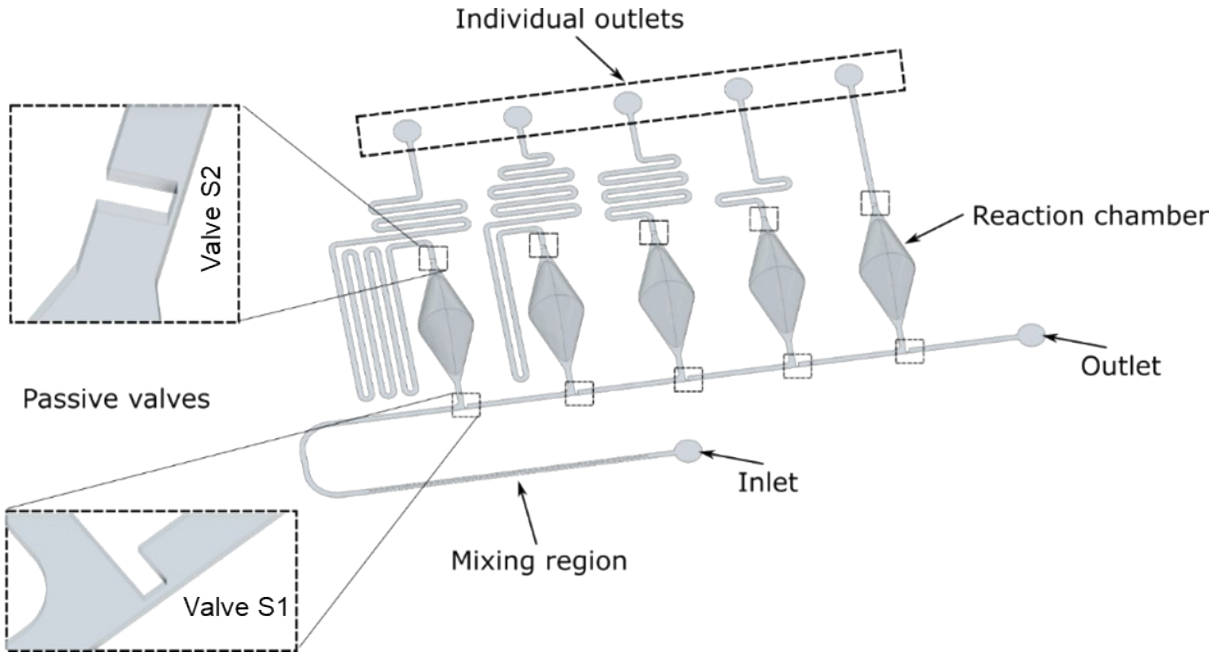

Figure S2. Detailed design of the microchannel and microchambers integrated with a pair of passive valves.

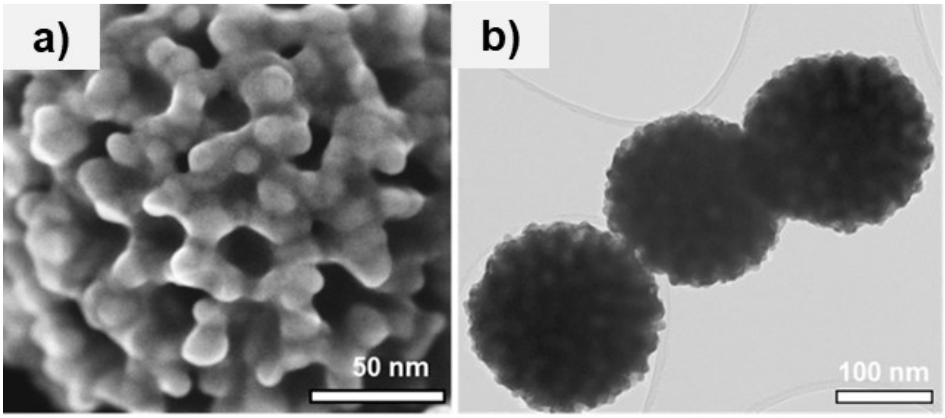

Figure S3. (a) High-resolution SEM image and (b) TEM image of mAuNPs.

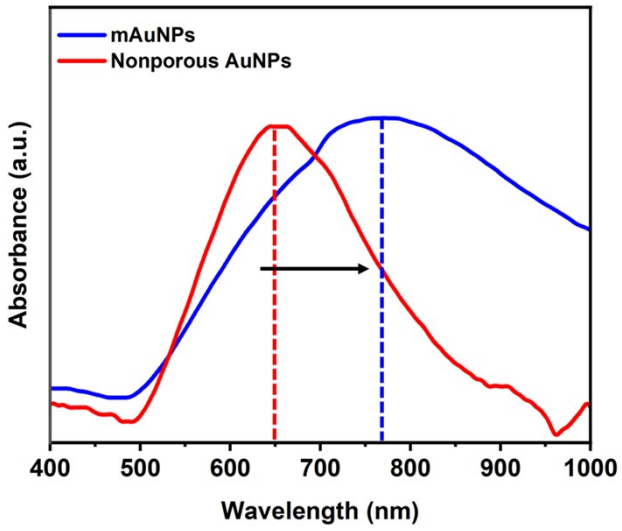

Figure S4. The UV-visible spectra of non-porous and mAuNPs (in water).

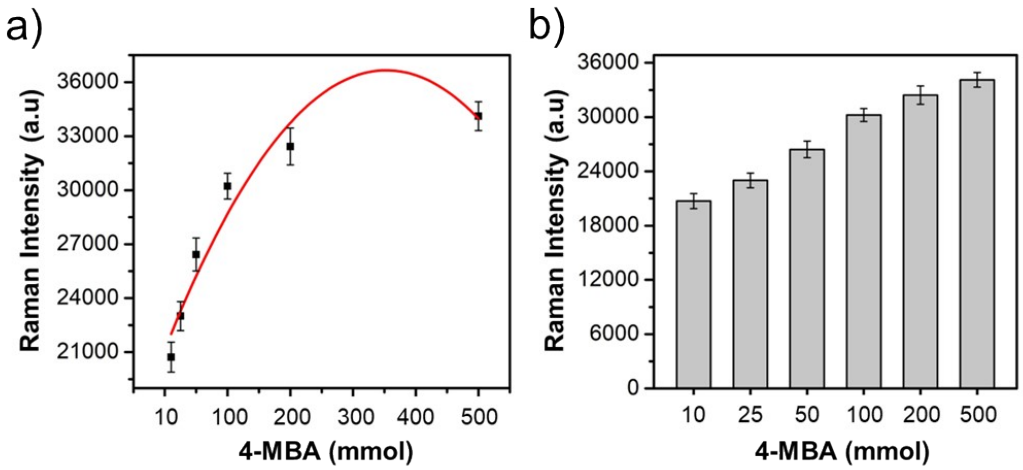

Figure S5. Optimization of the functionalization of mAuNPs with SERS molecule 4-MBA for achieving the most optimum signal. (a) Line curve of SERS response against different concentration of 4-MBA and (b) corresponding bar diagram. Error bars indicate standard deviation (SD) of three replicates for each concentration.

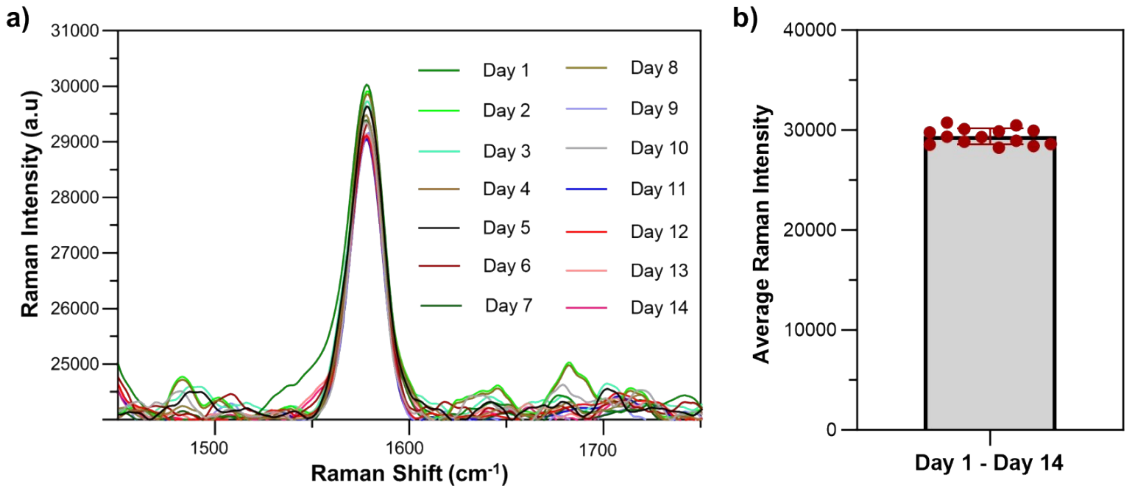

Figure S6. Time-dependent stability of the mAu/4-MBA SERS tag. (a) Each graph represents the characteristic Raman spectra of mAuNPs labeled with 4-MBA (SERS nanotags) until 14 consecutive days after synthesis. (b) Each red-colored data point represents the average Raman spectra of the mAuNPs nanotag for 14 consecutive days (RSD < 9%). Error bars indicate standard deviation (SD) of three replicates for each concentration.

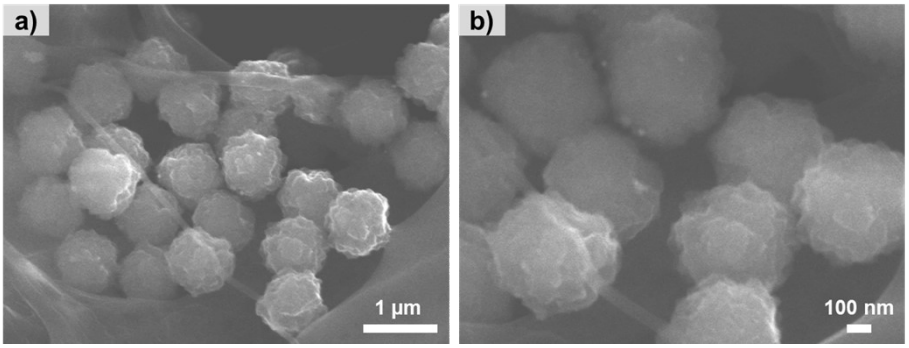

Figure S7. (a) SEM image of the mAuNPs nanotag present in the assay showing the random connection of the mAuNPs, and (b) enlarged view of the interconnected mAuNPs nanotags.

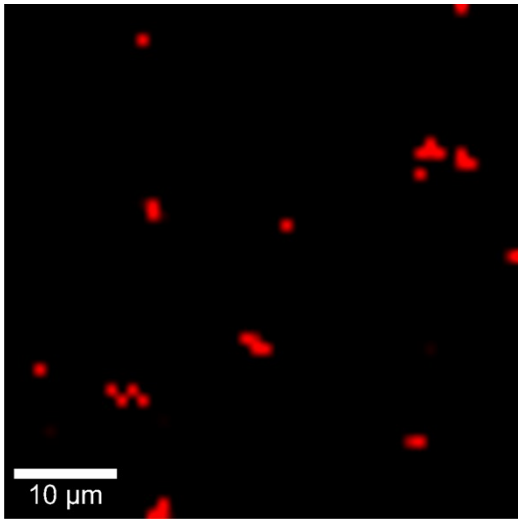

Figure S8. SERS mapping image of the assay using a Witec Raman AFM microscope (Laser wavelength = 633 nm; Magnification = 20X; Integration time (trace) (s) = 0.05; Geometry (Width × Height) = 60 × 60 µm; Image scan (points/line and points/image) = 60).

Table S1. Comparison of mAuNPs-Based SERS-Microfluidic Platform with other reports.

NPs	Target proteins	Detection principle	Assay sensitivity	Remarks/ Uniqueness	Ref.
Au NPs	RBD (SARS-CoV-2 & MERS-CoV-2)	▪ SERS performance because of Au NPs aggregation. ▪ Raman fingerprints of RBDs (structural and compositional) characteristics using machine learning.	-	It reported the fundamental optical properties of the SARS-CoV-2 RBD and the underlying SERS mechanism.	S1
Dendritic Ag	SARS-CoV-2 RNA	▪ High SERS performance because of dendritic structure with many tips. ▪ Detects the target RNA sequence of SARS-CoV-2 by Raman spectroscopy.	LOD = 7.42×10^{-14} M Linear range = 10^{-9} M–10^{-13} M	Dendritic Ag NPs were obtained by a one-click synthesis via integrated electrodeposition platform.	S2
Au NPs	SARS-CoV-2 spike protein (in saliva)	▪ High SERS performance is achieved using 2 assembled layers of Au NPs. ▪ Ag NPs were used as the SERS nanotags to qualitatively and quantitatively read out the SARS-CoV-2 spike protein.	LOD = 7.60 fg mL^{-1} (serum) and 0.10 pg mL^{-1} (blood)	The SERS activity of the substrates decorated with Au NPs was closely related to the number of assembled layers of Au NPs.	S3
Au NPs	SARS-CoV-2 spike protein aptamer	▪ The assay platform is based on one-step aptamer recognition using Raman spectroscopy. ▪ Au NPs were conjugated to the spike protein aptamer cocktail to ensure the SERS nanoprobes could selectively recognize virus particles and form sandwich structures.	LOD = 124 TU μL^{-1} (18 fM spike protein),	The assay exploited the high affinity binding with less steric hindrance on the coronavirus surface of aptamers and did not require virus pre-treatment.	S4

Au NPs	SARS-CoV-2 spike protein	▪ The SERS nanotags are based on 60 nm Au NPs. ▪ The high SERS performance is due to the binding affinity of single-chain Fv recombinant antibody fragments to the SARS-CoV-2 spike protein.	LOD = 257 fg mL^{-1}	This SERS-based immunoassay exploited the tendency of single chain Fv recombinant antibody to bind to SARS-CoV-2 spike protein.	S5
Ag@Au NPs	SARS-CoV-2 IgG	▪ High SERS performance is achieved through the synergistic effects from combining Au and Ag properties. ▪ The modification of the Ag@Au NPs with antibodies enabled them to recognize and combine with SARS-CoV-2 IgG, which was then captured by the SARS-CoV-2 spike protein.	LOD = 0.22 pg mL^{-1}	The Ag@Au NPs combines the unique surface chemistry of Au shell and the superior optical properties of the core Ag NPs. The nanogap between the Ag core and the Au shell also contributed to the enhanced Raman signal.	S6
Si NWs@Ag NPs	SARS-CoV-2 (RBD) spike protein	▪ Raman fingerprints of RBDs can be detected by the fabricated SiNWs/AgNPs sensor. ▪ High SERS performance is attributed to the binding of the Ag atoms on the sensor surface with the nitrogen atoms (N) of spike protein moiety.	LOD = 9.3×10^{-12} $molL^{-1}$	The immersion time in the decoration process of AgNPs onto Si NWs can be tuned to enhance the detection sensitivity toward the spike protein.	S7
AuNPs/COFs	SARS-CoV-2 spike protein	▪ A ternary “Y-shaped” aptasensor was incorporated onto the surface of a hybrid material consisting of Au NPs and covalent organic frameworks (COFs). ▪ The satisfactory SERS performance was due to the stable and high affinity of AuNPs/COFs substrate, as well as its uniform and densely packed “hotspots” between the Au@4-ATP@Ag@Au NPs and AuNPs/COFs substrates.	LOD = 2.7×10^{-16} g mol L^{-1} Linear range = 10^{-15} to 10^{-9} g mL^{-1}	The Y-shaped aptasensor reduced the distance between plasmonic NPs, which was beneficial to SERS detection.	S8
Ag NPs	SARS-CoV-2 spike and nucleocapsid proteins	▪ SERS platform based on variant-specific antibody-functionalized silver microplasma-engineered nanoassemblies (AgMEN).	LOD = 1 fg mL^{-1} (SARS CoV-2 spike protein)	The three-dimensional (3D) porous AgMEN provided high sensitivity and	S9

		▪ High SERS performance originated from the binding affinity of the antibodies functionalized on the Ag NPs and the spike and nucleocapsid proteins.	LOD = 0.1 pg mL^{-1} (SARS CoV-2 nucleocapsid protein)	could be designed to be selective toward a specific SARS-CoV-2 spike protein variant, such as wild-type, alpha, delta or omicron under simulated human saliva conditions.	
Fe_3O_4-Ag^{MBA}@ Au NPs	SARS-CoV-2 nucleocapsid protein	▪ High SERS performance is achieved as a result of the signal enhancement by Ag@Au NPs, while the Fe_3O_4 NPs could minimize interference from the matrix.	LOD = 0.08 pg mL^{-1}	The Fe_3O_4-Ag^{MBA}@Au NPs modified with the nucleocapsid protein could be used as a dual colorimetric-SERS detection.	S10
mAuNPs	SARS-CoV-2 S1, RBD and NCD Proteins.	▪ High SERS response due to mesoporous structure of Au NPs. ▪ Multiplexed platform for simultaneous detection of 3 different spike proteins.	LOD = 14 pg mL^{-1}	This platform offers a multiplexed system for detecting 3 different spike proteins along with 2 controls, providing high specificity and accuracy. Moreover, multiplexing enables the use of this platform outside of laboratories.	This work

References

(S1) K. Zhang, Z. Wang, H. Liu, N. Perea-López, J. C. Ranasinghe, G. Bepete, A. M. Minns, R. M. Rossi, S. E. Lindner, S. X. Huang, M. Terrones, *ACS Photonics*, 2022, **9**, 2963-2972.

(S2) Z. Li, Y. Luo, Y. Song, Q. Zhu, T. Xu, X. Zhang, *Anal. Chim. Acta*, 2022, **1234**, 340523.

(S3) M. Zhang, X. Li, J. Pan, Y. Zhang, L. Zhang, C. Wang, X. Yan, X. Liu, G. Lu, *Biosens. Bioelectron*. 2021, **190**, 113421.

(S4) P. C. Guan, H. Zhang, Z. Y. Li, S. S. Xu, M. Sun, X. M. Tian, Z. Ma, J. S. Lin, M. M. Gu, H. Wen, F. L. Zhang, *Anal. Chem*., 2022, **94**, 17795-17802.

(S5) D. Antoine, M. Mohammadi, M. Vitt, J. Dickie, S. S. Jyoti, M. A. Tilbury, P. A. Johnson, K. E. Wawrousek, J. G. Wall, *ACS Sensors*, 2022, **7**, 866-873.

(S6) P. Liang, Q. Guo, T. Zhao, C. Y. Wen, Z. Tian, Y. Shang, J. Xing, Y. Jiang, J. Zeng, *Anal. Chem*., 2022, **94**, 8466-8473.

(S7) K. Daoudi, K. Ramachandran, H. Alawadhi, R. Boukherroub, E. Dogheche, M. A. El Khakani, M. Gaidi, *Surf. Interfaces,* 2021, **27**, 101454.

(S8) Y. Xie, Q. Li, J. Chen, W. Yue, Z. Xia, M. Zeng, Y. He, Y. Zhao, X. Luo, *Sens. Actuators B Chem*., 2023, **394**, 134470.

(S9) Y. J. Yeh, T. N. Le, W. W. W. Hsiao, K. L. Tung, K. K. Ostrikov, W. H. Chiang, *Anal. Chim. Acta,* 2023, **1239**, 340651.

(S10) J. Li, P. Liang, T. Zhao, G. Guo, J. Zhu, C. Wen, J. Zeng, *Anal. Bioanal. Chem*., 2023, **415**, 545-554.